electronics

Article

Sustainable Floating PV–Storage Hybrid System for Coastal Energy Resilience

Yong-Dong Chang [1], Gwo-Ruey Yu [2,*], Ching-Chih Chang [1] and Jun-Hao Chen [1]

[1] Department of Electrical Engineering, National Penghu University of Science and Technology, Magong City 88046, Taiwan; ydc0523@gms.npu.edu.tw (Y.-D.C.); d12417008@ems.npu.edu.tw (C.-C.C.); d12417016@ems.npu.edu.tw (J.-H.C.)
[2] Department of Electrical Engineering, National Chung Cheng University, Chiayi 62102, Taiwan
* Correspondence: ieegwoyu@ccu.edu.tw

Abstract

Floating photovoltaic (FPV) systems are promising for coastal aquaculture where reliable electricity is essential for pumping, oxygenation, sensing, and control. A sustainable FPV–storage hybrid tailored to monsoon-prone sites is developed, with emphasis on energy efficiency and structural resilience. The prototype combines dual-axis solar tracking with a spray-cooling and cleaning subsystem and an active wind-protection strategy that automatically flattens the array when wind speed exceeds 8.0 m/s. Temperature, wind speed, and irradiance sensors are coordinated by an Arduino-based supervisor to optimize tracking, thermal management, and tilt control. A 10 W floating module and a fixed-tilt reference were fabricated and tested outdoors in Penghu, Taiwan. The FPV achieved a 25.17% energy gain on a sunny day and a 40.29% gain under overcast and windy conditions, while module temperature remained below 45 °C through on-demand spraying, reducing thermal losses. In addition, a hybrid energy storage system (HESS), integrating a 12 V/10 Ah lithium-ion battery and a 12 V/24 Ah lead-acid battery, was validated using a priority charging strategy. During testing, the lithium-ion unit was first charged to stabilize the control circuits, after which excess solar energy was redirected to the lead-acid battery for long-term storage. This hierarchical design ensured both immediate power stability and extended endurance under cloudy or low-irradiance conditions. The results demonstrate a practical, low-cost, and modular pathway to couple FPV with hybrid storage for coastal energy resilience, improving yield and maintaining safe operation during adverse weather, and enabling scalable deployment across cage-aquaculture facilities.

Keywords: floating photovoltaic; dual-axis solar tracking; spray cooling; wind protection; coastal energy resilience; hybrid energy storage system

check for updates

Academic Editor: Arian Zahedmanesh

Received: 1 September 2025
Revised: 3 October 2025
Accepted: 6 October 2025
Published: 7 October 2025

Citation: Chang, Y.-D.; Yu, G.-R.; Chang, C.-C.; Chen, J.-H. Sustainable Floating PV–Storage Hybrid System for Coastal Energy Resilience. *Electronics* **2025**, *14*, 3949. https://doi.org/10.3390/electronics14193949

Copyright: © 2025 by the authors. Licensee MDPI, Basel, Switzerland. This article is an open access article distributed under the terms and conditions of the Creative Commons Attribution (CC BY) license (https://creativecommons.org/licenses/by/4.0/).

1. Introduction

Cage aquaculture is an efficient marine farming method that uses large floating buoys and net-cage structures to concentrate fish within defined marine areas for precise stock management and growth monitoring. The cages' permeable design both shields stock from external disturbances and promotes seawater exchange and oxygen transport. In Penghu (23.57° N, 119.58° E), an offshore island county of Taiwan located in the Taiwan Strait, more than 2000 cages, as shown in Figure 1, produce several hundred to several thousand tons annually across species such as grouper, sea bass, eel, clams, and scallops, underscoring the sector's regional importance. Penghu's cage-aquaculture environment

and planning foundations can be linked through three complementary studies by Shih [1–3]: first, Shih visualized benthic redox-potential and sulfide profiles beneath and around cobia cages, revealing a reduction gradient indicative of seabed conditions that support stable operations. Second, Shih combined GIS with analytic hierarchy process (AHP), a multi-criteria decision-making method, to rank Penghu coves by multi-criteria suitability—hydrodynamics, depth, accessibility, water quality, and use conflicts—thereby providing a replicable siting tool for marine aquaculture. From a governance perspective, Shih then outlined development and environmental-management strategies for Taiwan's cobia industry, including zoning, monitoring, waste handling, and disease and feed management. Complementing these foundations, Lan et al. evaluated the investment feasibility of large submersible cage culture for snubnose pompano and cobia in Taiwan [4], and Tang et al. assessed the engineering feasibility of deploying cage aquaculture within offshore wind-farm areas around Taiwan [5]. Collectively, this body of work supports Penghu's competitive, high-quality cage-aquaculture sector that meets strong local demand and contributes to export markets.



Figure 1. Offshore cage aquaculture in Penghu bay.

However, the aquaculture industry also faces several challenges. First, according to the study by Sievers et al. [6], pump systems are crucial in the aquaculture process as they maintain water circulation and oxygenation, ensuring that fish receive adequate oxygen and a steady flow of fresh water. Secondly, oxygenation facilities such as aeration stones and oxygenators directly affect the oxygen concentration in the water and require a stable power supply to function effectively. These power-driven systems improve the efficiency and output of cage aquaculture. They also play a vital role in maintaining the environment and the health of organisms during farming. Additionally, lighting systems are important for regulating the growth cycles and behavior of aquatic species, especially in winter or higher latitudes. Monitoring facilities, such as cameras and sensors, provide valuable data to help monitor and manage the health of organisms and water quality within the cages. Temperature control systems play a critical role in regulating water temperature and adapting to climate change, and these functions rely on a stable power supply. Bujas et al. [7] discussed how renewable energy can improve the environmental sustainability of the aquaculture industry. Their study highlighted its effectiveness in addressing power supply challenges in cage aquaculture and in ensuring proper management and long-term sustainability of farming operations. Adoption of solar power systems has become a clear trend, with relevant studies including the following: Vo et al. outlined solar applications for aquaculture—including aeration, pumping, sensing, and monitoring—and synthesized adoption barriers and near-term trends [8]. Vivar et al. reviewed photovoltaic use in water-related technologies, mapping configuration choices, performance trade-offs,

and environmental aspects to guide system design [9]. Gorjian et al. surveyed FPV technical advances, economics, and environmental impacts with emphasis on deployment in space-constrained sites [10]. Guo et al. traced global aquavoltaics trends, highlighting co-benefits between electricity generation and aquaculture and emerging policy/technology pathways [11]. Nisar et al. experimentally showed that FPV lowers module temperature and boosts energy yield relative to ground-mounted systems, with added evaporation suppression [12]. Manolache et al. evaluated the economic feasibility of floating solar and its integration with marine renewables, aquaculture, and hydrogen, reporting indicative LCOE ranges and design implications [13]. Collectively, these studies indicate that FPV can deliver reliable electricity while reducing operating costs and environmental impacts. FPV also helps overcome space constraints, enhance energy utilization, and maintain cage stability against wave action. However, careful attention must still be given to conversion efficiency and site-specific constraints. Silicon modules remain the mainstream choice, but their performance exhibits negative temperature dependence: Segbefia profiled 20-year-old field-aged multicrystalline silicon modules and showed that elevated operating temperatures—exacerbated by optical degradation—coincide with output loss, confirming that efficiency declines as cell temperature rises [14]. To mitigate temperature-driven losses, recent work spans thermosiphon cooling tailored for FPV [15], comprehensive reviews of passive/active PV cooling [16], and FPV design solutions that influence thermal behavior and yield [17]. New field evidence consistent with a 2–5 °C operating-temperature reduction shows that canal-mounted PV panels ran on average 4.2 °C cooler (up to 6.33 °C) than ground-mounted panels in controlled experiments [18], while a floating PV study benchmarking FPV against land-based PV reported >2 °C reductions under specific configurations [19]. In waterside deployments—floating and canal-top—a thin water film or spray combined with passive thermosiphon action or a short-loop pump circuit can further enhance heat rejection, with relatively simple hardware requirements [15,16,18]. Active cooling methods can increase power generation by 12% to 18%. Research by Tashtoush and Al-Oqool [20] indicates that maintaining an optimal module cooling temperature of 37 °C with minimal evaporation loss can improve energy output by 15.28% to 17.75%. Additionally, PV modules are prone to soiling—accumulation of dust, bird droppings, and sea-salt deposits—which depresses conversion efficiency; routine surface cleaning is therefore a critical maintenance task, as documented in [21–24].

Furthermore, the Penghu region, located in the middle of the Taiwan Strait, experiences active northeast monsoon winds from November to March each year. These winds, originating from the Siberian high-pressure system, blow from the north or northeast [25], resulting in higher wind speeds and colder, drier air that affects both Penghu and the western part of Taiwan. According to the above, the research focuses on maximizing energy harvest by integrating collection, cooling, dust-removal, and wind-protection mechanisms into a single, enhanced floating solar-tracking system. The proposed design incorporates several key features. First, it includes a cost-effective and easy-to-implement cooling subsystem with a simple structure and low maintenance requirements. Second, it provides a multi-functional active maintenance module capable of cooling, removal of dust and salt fog, bird-dropping cleaning, and emergency fire suppression to enhance photovoltaic conversion efficiency. Finally, it integrates an active wind-protection capability that leverages solar tracking to adjust the platform's attitude during typhoons or northeast monsoons, thereby reducing the risk of large-scale capsizing.

The remarkable features of this research encompass its significant contributions to the following aspects:

- Increased Power Output: By incorporating a solar-tracking mechanism, the system significantly outperforms fixed floating panels across a range of irradiance conditions.

- Optimized Cooling Strategy: Introducing a low-cost active cooling solution with dust and salt crystal removal capabilities to reduce module temperature and thereby enhance overall conversion efficiency.
- Enhanced Structural Safety: An active wind-protection design is integrated to substantially reduce the risk of platform overturning during extreme weather events.
- Broad Applicability: The cooling system and wind protection features can be retrofitted to land-based or floating fixed solar installations, making them highly suitable for large-scale deployment.
- Hybrid Energy Storage System (HESS): A lithium-ion and lead-acid hybrid storage architecture with a priority-charging strategy is incorporated, ensuring immediate circuit stability and long-term energy backup under cloudy or low-irradiance conditions, thereby strengthening system resilience.

The remainder of the paper is organized as follows. In Section 2, the characteristics of the employed solar cells are reviewed. Section 3 describes the fabrication process of the proposed floating-solar power system. Section 4 presents the measured performance and provides the corresponding discussion. Finally, Section 5 provides the study conclusion.

2. Solar Cell Characteristics

A solar cell is a device that converts solar energy into electrical energy. Unlike systems that rely on electrolytes to conduct electric ions, solar cells use semiconductor PN junctions to generate potential. The working principle involves the absorption of sunlight by the solar cell, where the energy of the photons is transferred to the conduction band electrons in the N-type silicon layer, causing them to become free and generate a large number of free electrons. The movement of these electrons produces a photocurrent, creating a potential difference at the PN junction. This process is illustrated in the equivalent circuit diagram shown in Figure 2 [26].

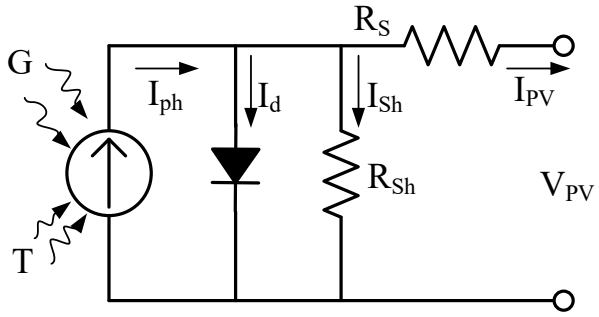


Figure 2. Equivalent circuit diagram of a solar cell.

The energy conversion of photovoltaic solar cells primarily relies on the photovoltaic effect of the PN junction. Based on the equivalent circuit shown in Figure 2, the following equations can be derived to describe this behavior [26].

$$I_{pv} = I_{ph} - I_d - I_{sh} \tag{1}$$

$$I_{pv} = I_{ph} - I_S\left[\exp\left(\frac{V + IR_s}{nV_T}\right) - 1\right] - \left[\frac{V + IR_s}{R_{sh}}\right] \tag{2}$$

$$I_{pv} = \left[I_{scr} + K_i\left(T_c - T_{ref}\right)\right]\frac{G}{G_{ref}} \tag{3}$$

where I_{scr} is the solar cell short-circuit current [A], K_i is the short-circuit current temperature coefficient [A/°C], T_{ref} is the reference temperature [°C], T_c is the cell operating temperature [K], I_s is the reverse saturation current of the solar cell [A], G is the solar insolation [W/m^2],

G_{ref} is the reference solar insolation [W/m^2], and $V_T = \frac{kT_b}{q}$ is the thermal voltage (25.68 mV at 300 K) [V], where k is the Boltzmann constant (1.38×10^{-23} J/K), q is the electron charge (1.602×10^{-19} C), and n is the diode ideality factor (typically between 1 and 2). Note that in some references, the operating temperature is denoted as T_b, which is equivalent to T_c expressed in Kelvin. In addition, variations in temperature affect the saturation current I_S of the cell, and this relationship can be expressed by the following equation [26].

$$I_S = I_o \left(\frac{T_c}{T_{ref}} \right)^3 \exp \left[\frac{qE_g}{nk} \left(\frac{1}{T_{ref}} - \frac{1}{T_c} \right) \right] \tag{4}$$

where I_o is the cell reverse saturation current under standard conditions at 25 °C and 1000 W/m^2 [A], E_g is the band-gap energy of the Si solar cell with a value of 1.1 eV, and n is the series cell number. The reverse saturation current at the reference temperature can be approximately obtained from the following equation [26].

$$I_o = \frac{I_{sc}}{\exp\left(\frac{qV_{oc}}{nkT_c}\right)} - 1 \tag{5}$$

Several solar cells are connected in series to form a solar module. Multiple solar modules are then combined in series and/or parallel configurations to create a solar array, tailored to meet the requirements of different loads. In the solar array power system, the energy generated (E_d) is represented by the total daily recorded output power [27], as shown in Equation (6), where E_d is expressed in watt-hours (Wh).

$$E_d = \sum_{t=1}^{t=Tip} P_{O,a} \times T_i \tag{6}$$

The energy generated each month is represented by Equation (7) [27]:

$$E_m = \sum_{d=1}^{N} E_d \tag{7}$$

where T_i represents the recording time interval [s], T_{ip} denotes the reporting period [h], N is the number of operational days of the solar modules per month, and $P_{O,a}$ is the output power [W], as specified in Equation (8) [27]:

$$P_{O,a} = V_{pv,a} \times I_{pv,a} \tag{8}$$

The yield (Y_f) of the solar array power system corresponds to the total energy (E_{ac}) [kWh] generated per installed nominal power ($P_{O,a}$) of the solar power array system, expressed in kilowatts peak [kWp]. This value represents the number of hours the solar power module should operate at its rated power $P_{O,m(rated)}$ [kW]. The daily final efficiency (Y_f, d) [h/day] and monthly final efficiency (Y_f, m) [h/month] are given by the following equations [27]:

$$Y_{f,d} = \frac{E_{ac,d}}{P_{O,m(rated)}} \tag{9}$$

and

$$Y_{f,m} = \left(\frac{1}{N} \right) \times \sum_{d=1}^{N} Y_{f,d} \tag{10}$$

Figure 2 illustrates that the optimal operating temperature range is between 0 °C and 75 °C. The P-V characteristics represent the relationship between output power and output

voltage while maintaining constant solar irradiance (G) [W/m^2] and temperature (T) [°C]. The effect of temperature on the solar module's electrical efficiency can be analyzed using the following equation [27]:

$$\eta_{pv} = \eta_{TR}\left[1 - \beta_R(T_C - T_R) + \gamma \log_{10} I_{pv}\right] \quad (11)$$

where η_{PV} is the solar module efficiency measured at the reference temperature; T_R (25 °C); βR is the temperature coefficient of module efficiency [1/°C] (typically ranging from 0.004 to 0.005/°C); I_{PV} is the average irradiance incident on the solar module per hour at the nominal operating temperature [W/m^2]; T_C represents the temperature of the solar component [°C]; and Y is the radiation intensity coefficient of the module efficiency, which is commonly assumed to be zero.

Based on the above, this modeling framework is not intended to provide stand-alone numerical results, but rather to establish the theoretical baseline for interpreting the experimental data. It enables the quantification of expected thermal and electrical behaviors under varying irradiance and temperature conditions, and serves as a benchmark against which the measured performance improvements of the FPV system are validated.

3. Fabrication of Proposed Floating Solar Power System

To implement the floating solar-tracking system, the layout shown in Figure 3 was adopted [28–30]. Natarajan et al. [28] demonstrated a dual-axis tracking FPV prototype with a controller–actuator arrangement suitable for floating deployment. Their design provided information on the controller, battery, drive stages, and two-dimensional mechanism. On the left, the control board integrates a no-fuse breaker (NFB), a 12 V lithium battery, drive circuitry, an Arduino module, and a wind-speed sensor. The drive set comprises the underwater motor, a telescoping rod, and the spraying subsystem. On the right, the solar-module section includes the module, carrier platform, two-dimensional mechanical system, the underwater motors, and the spray line. Figure 4 presents the system architecture and its hardware mapping. The left panel shows the functional block diagram, with the Arduino module at the core linking four subsystems—solar tracking, wind-protection, spray cooling, and night-return—and exchanging signals among them. The right panel depicts the controller prototype powered via a fused switch and a 12 V Li-ion battery; driver boards interface the underwater motors, the telescopic actuator, and the spray line, while sensors (e.g., anemometer) feed real-time data to the controller. Based on these inputs, the Arduino executes tracking, high-wind protection, and cleaning/cooling routines. The modular layout simplifies maintenance and future expansion.

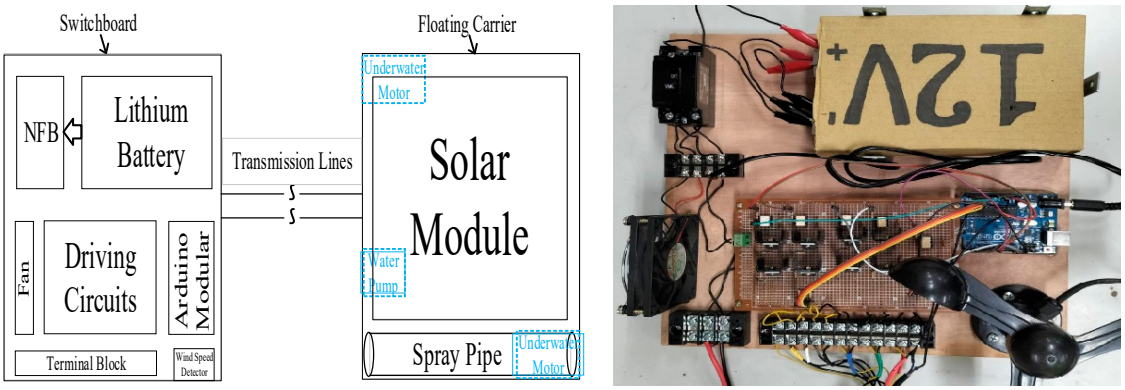


Figure 3. Floating solar-tracking photovoltaic (FPV) system: (**a**) Functional system layout; (**b**) Prototype hardware setup.

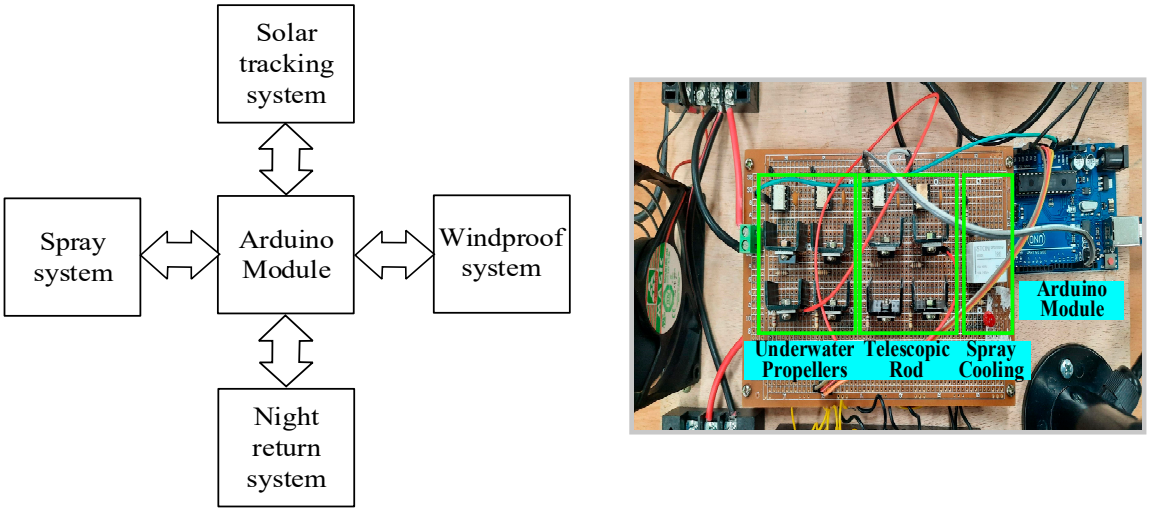


Figure 4. Overview of the floating solar-tracking system: (**a**) Functional block diagram of FPV subsystems and their interactions; (**b**) Prototype Arduino-based controller and driver circuitry.

3.1. Centralized Control and Driving Circuit for the Solar-Tracking System

Optimal performance of the solar-tracking system is achieved using an Arduino module as the central control unit. It manages the operation of the underwater motors and telescopic rods. The corresponding driving circuit diagram is shown in Figure 5. Figure 5 only shows the circuit for the underwater motor, while the circuits for the solar tracking and spray systems are the same. To accurately detect changes in sunlight intensity, the system employs Light Dependent Resistors (LDRs), as shown in Figure 5 from LDR1 to LDR4. Among them, LDR1 and LDR2 are responsible for the tracking function of the carrier platform, while LDR3 and LDR4 are responsible for the tracking function of the solar panel's tilt angle. Taking the carrier platform tracking function as an example, when the light sensors LDR1 and LDR2 detect changes in solar radiation, the light signal is converted into a voltage signal, which is then transmitted to the A0 and A1 input ports of the Arduino module for signal processing. After processing the signal internally, the Arduino outputs the result to Pin 12 and Pin 13, which are connected to the full-bridge circuit. Based on the received signal, the full-bridge circuit controls the forward and reverse rotation of the underwater motor under the carrier platform. This ensures that the carrier platform solar-tracking system can accurately follow the sun's position, maximizing solar energy collection. The implementation diagram of Figure 5 is shown in Figure 4b above. This configuration utilizes TLP250 optocoupler drivers and Metal-Oxide-Semiconductor Field-Effect Transistors (MOSFETs) to control the underwater motors, telescopic rods, and water pumps. The TLP250 converts the 5 V PWM control signals from the Arduino into 12 V gate-drive pulses, providing both optical isolation and gate-voltage amplification. The TLP250 device located near the Arduino UNO drives transistors Q1 and Q4 simultaneously, while the other TLP250 controls Q2 and Q3. By alternately switching these transistor pairs, the full-bridge circuit enables bidirectional current flow through the underwater motor, allowing forward and reverse rotation. This configuration enhances driving capability, ensures fast switching speed, reduces electrical noise, and provides stable and efficient operation between the low-voltage control circuit and the high-current power stage.

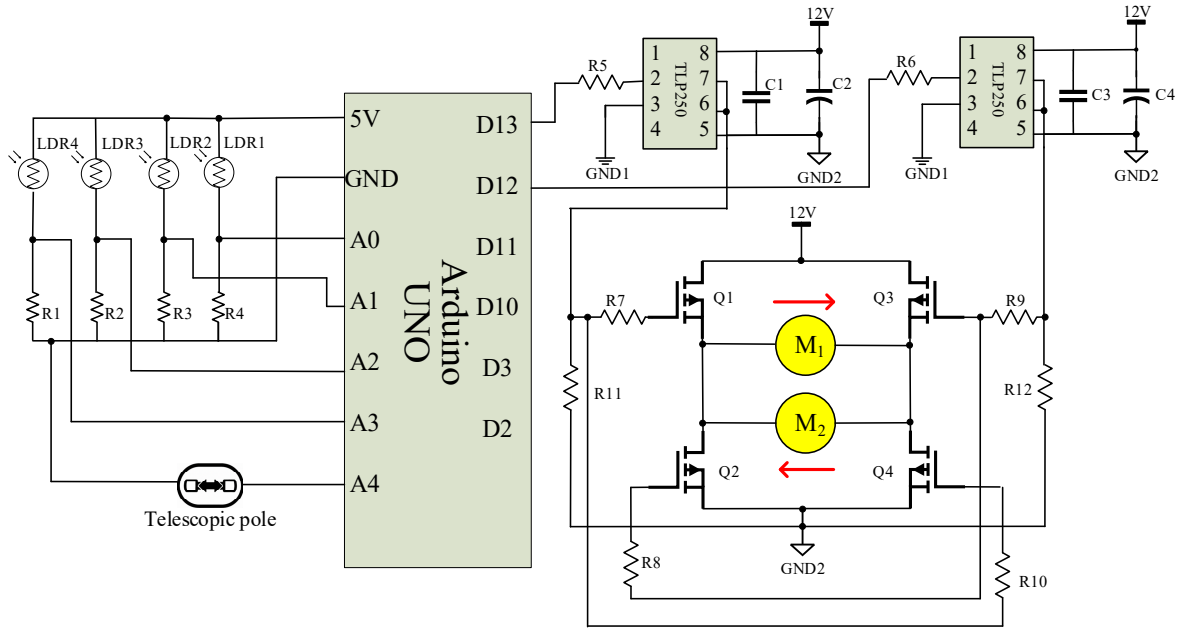


Figure 5. Block diagram of the Arduino module combined with full bridge circuit.

3.2. Windproof System

The anemometer is designed to measure the wind speed of the environment, as illustrated in Figure 6. When the surrounding environment experiences wind, the cups on the device start to rotate, which drives an internal generator to produce a voltage. This voltage data can be used by the Arduino module for control purposes.



(**a**) (**b**)

Figure 6. Wind-speed sensor and verification setup: (**a**) Anemometer; (**b**) Functional-verification test, where the arrows indicate that when the wind speed reaches the preset threshold, the anemometer cups rotate and the solar panel tilts downward to a horizontal position.

When the wind speed exceeds 8.0 m/s, classified as a Fresh Breeze according to Table 1, the system retracts the modules to a horizontal orientation to prevent overturning. The relationship between the wind speed sensor's output voltage signal and wind speed is given by:

$$F = 27 \times V \tag{12}$$

where F is the wind speed in meters per second (m/s), and V is the output voltage, expressed in volts (V).

Table 1 summarizes the relationship between wind scale, corresponding wind speed, and the expected influence on PV module performance. As wind speed increases, convective cooling becomes more effective, helping to lower module surface temperature and

maintain higher efficiency. However, once the wind speed exceeds 8.0 m/s (classified as Fresh Breeze), the system's automatic protection mechanism adjusts the solar module to a horizontal position, reducing power generation to ensure structural stability. At Strong Breeze levels, power tracking is suspended entirely, limiting energy yield.

Table 1. Wind Speed Levels for PV Module Wind Protection Design.

Wind Scale	Name	Wind Speed (m/s)
0	Calm	0.0–0.2
1	Light air	0.3–1.5
2	Light breeze	1.6–3.3
3	Gentle breeze	3.4–5.4
4	Moderate breeze	5.5–7.9
5	Fresh breeze	8.0–10.7
6	Strong breeze	10.8–13.8

3.3. Monocrystalline Silicon Solar Module

Monocrystalline, polycrystalline, and amorphous silicon solar modules are all common materials, each differing in structure and manufacturing processes, which impact their performance and applications. Monocrystalline silicon modules are made from a single crystal of silicon. During their production, a single crystal is pulled from molten silicon, resulting in a uniform crystalline structure that offers higher performance and efficiency. Although they tend to be more efficient, they are also more costly to manufacture. Polycrystalline silicon modules, on the other hand, are composed of multiple silicon crystals. The manufacturing process for these modules is more economical compared to monocrystalline modules, as the structure of the polycrystalline silicon is less orderly. Consequently, while their performance and efficiency are generally lower, the cost is reduced. Polycrystalline modules are among the most widely used solar modules today. Amorphous silicon modules use a non-crystalline, disordered silicon material. Their manufacturing process is simpler, which lowers the cost, and they can be produced in flexible forms, making them suitable for applications such as building-integrated photovoltaics. However, amorphous silicon modules typically have lower performance and efficiency and are subject to performance degradation over time. For the convenience of functional verification and high efficiency considerations, this study selected a 10 W solar module, the specifications are listed in Table 2, and its appearance is shown in Figure 7.



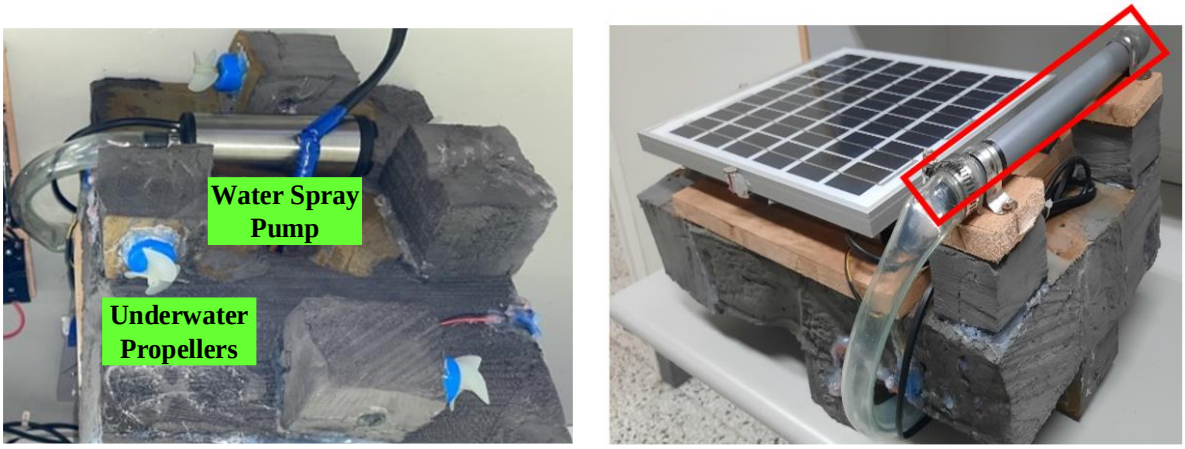
Figure 7. The monocrystalline solar module.

Table 2. PV module electricity performance parameters.

Item	Type	Parameter
1.	Rated power	10 W
2.	Rated voltage	17.5 V
3.	Rated current	0.57 A
4.	Open circuit voltage	21.5 V
5.	Short circuit current	0.65 A
6.	Operating voltage and current temperature coefficient	–0.33%/°C and 0.08%/°C
7.	Operating temperature	–40 to +85 °C
8.	Efficiency	≥10%
9.	Dimension	35 × 27 × 1.8 cm

3.4. Spray Cooling System

The abundant water source is a significant advantage for floating solar modules. By utilizing a spray pump system, as shown in Figure 8a, water can be drawn from beneath the system to achieve cooling and cleaning purposes. The spray cooling system consists of a water pump, PVC pipes, relay circuits, and temperature sensors. The DS18B20 temperature sensor installed on the backside of the solar module monitors the surface temperature. When the temperature reaches 45 °C, it sends a signal to the Arduino module, which activates the relay to start the spray cooling system. This will activate the relay and subsequently start the spray cooling system. Water beneath the system is pumped through pipes and then sprayed onto the solar module via the PVC pipes, as shown in Figure 8b. This process helps to cool and clean the solar module. The spraying continues until the module temperature drops to 35 °C. The advantage of this cooling system lies in its simple structure, low cost, ease of maintenance, and the ability to be deployed on a large scale without complex components.



(**a**) (**b**)

Figure 8. Water-spray cooling system: (**a**) Water pump and underwater propellers; (**b**) PVC spray header mounted on the solar module.

3.5. Software Development

The system operation flowchart is illustrated in Figure 9. Based on this flowchart, the Arduino module software (Arduino IDE version 1.8.19) is developed. Upon initialization, the program receives signals from the photoresistor, anemometer, and temperature sensor.

Using this data, the software adjusts the tracking functions of the underwater motor and retractable arm, as well as monitors the surrounding wind speed and the temperature of the solar module. The tracking function is set to execute every 5 min, aiming to prevent the underwater motor from continuously tracking the sun, which would consume more power, thereby minimizing energy loss during the continuous tracking period. When the solar module voltage drops below 10 V, indicating sunset, the system will stop the tracking function as it transitions to night time mode. If the anemometer detects wind speeds exceeding level 5 (8.0 m/s), the system switches to high-wind mode. It forces the retractable arm to lower the solar module to a horizontal position, thereby reducing wind resistance and the risk of overturning. Additionally, considering that the outdoor ambient temperature can easily cause the solar panels to reach 35 °C, leading to the spray system being activated too frequently, the temperature of the solar panels is set to 45 °C. This effectively prevents excessive power consumption while allowing the spray cooling system to lower the temperature of the module.

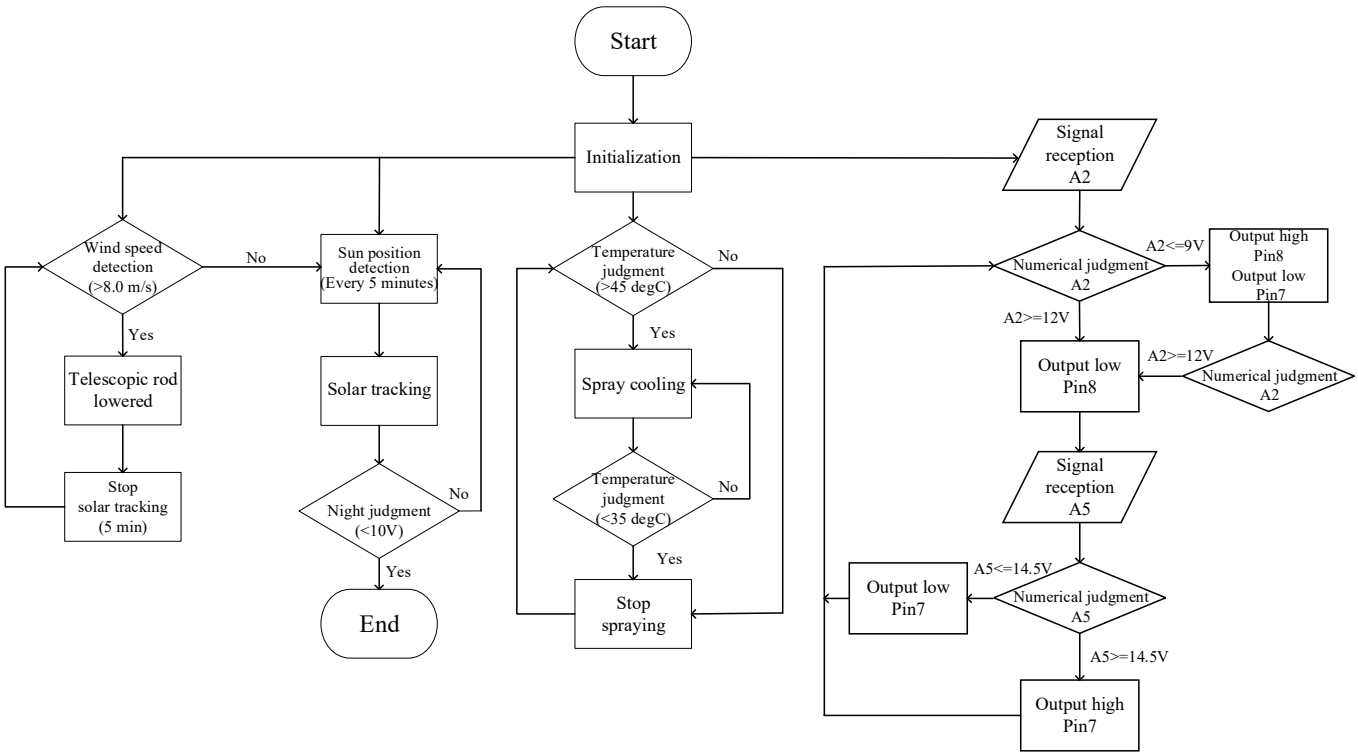


Figure 9. Flowchart of the proposed solar system's operation.

To ensure a stable power supply for the driving circuits, the proposed system employs a hybrid energy storage system (HESS) that integrates both a lithium-ion battery and a lead-acid battery. A priority charging strategy is implemented to optimize solar energy utilization and balance the operational roles of the two storage devices. Specifically, the lithium-ion battery is configured to provide a regulated 12 V output, thereby protecting the sensitive electronic components of the driving circuit from voltage fluctuations. In contrast, the lead-acid battery serves as the main energy reservoir, with its maximum charging voltage set to 14.5 V. The control logic is implemented through the Arduino module. Analog pins A2 and A5 are assigned to continuously monitor the voltages of the lithium-ion and lead-acid batteries, respectively. Based on the monitored values, digital pins 7 and 8 generate switching control signals to regulate the charging pathways. Under normal conditions, the system prioritizes charging the lithium-ion battery to secure a stable supply for the control and actuator circuits. Once the lithium-ion battery reaches its

nominal voltage, the charging current is redirected to the lead-acid battery for long-term energy storage. This hierarchical approach not only improves the overall utilization of solar energy but also enhances the endurance and operational safety of the FPV platform under variable irradiance conditions.

4. Measured Results and Discussion

This section details the post-assembly functional testing, including indoor verification and outdoor performance evaluation. In the field trials, the proposed floating solar-tracking system was benchmarked against a fixed ground-mounted reference; their power/energy outputs and relevant parameters were measured under sunny and overcast conditions, and the observed differences were subsequently analyzed and discussed.

4.1. System Hardware Development and Functional Verification

The prototype system for the floating solar power generation, which integrates both software and hardware, is illustrated in Figure 10. The platform comprises a floating PV module deployed in a water tank and a benchtop controller module, as shown in Figure 10a. Indoor tests validated the solar-tracking, spray-cooling, and wind-protection functions, as shown in Figure 10b–d. The proposed system is powered by a 12 V/10 Ah lithium-ion battery pack and operates stably in a standalone, self-contained mode without any external power supply.

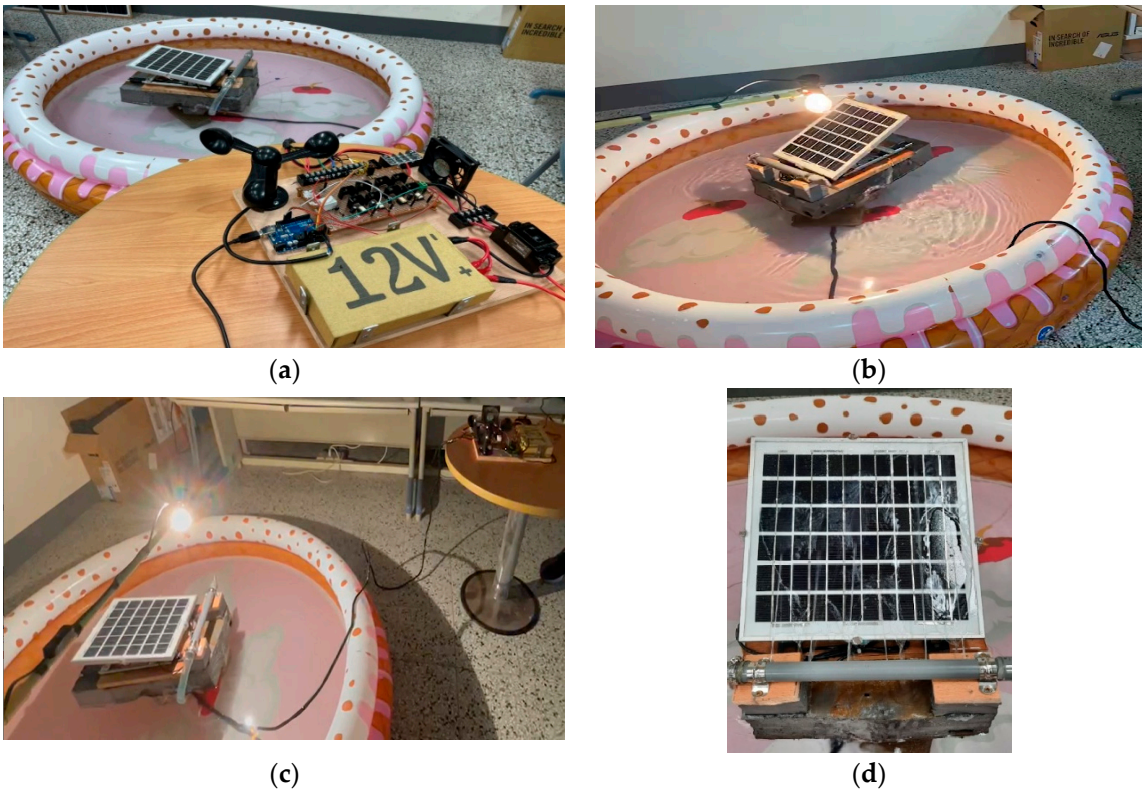


Figure 10. Prototype validation of the floating solar-tracking system: (**a**) Floating solar-tracking prototype; (**b**) Solar-tracking test; (**c**) Wind-protection test; (**d**) Spray-cooling test.

4.2. Measurement Results

In the laboratory, a halogen lamp was used as an artificial radiation source for preliminary functional verification of the FPV tracking and control circuits. For performance evaluation, the system was tested under natural outdoor solar irradiance in Penghu, Taiwan (23.57° N, 119.58° E). The irradiance was recorded with a pyranometer at a 20 s sampling

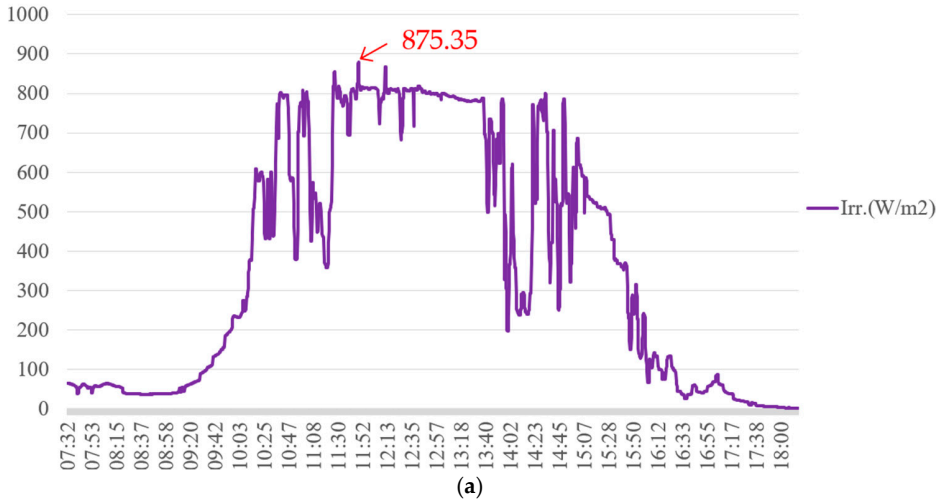
interval. Representative irradiance profiles for sunny and cloudy conditions are shown in Figure 11a and Figure 12a, respectively. For comparison, a ground-fixed system with an inclination angle of 23° was also fabricated and tested alongside the floating system. The spray cooling system was activated at a temperature of 45 °C, with sampling intervals of 20 s. The data logger recorded multiple parameters, including voltage, current, solar module temperature, and ambient temperature for both the floating and ground-fixed systems. Table 3 provides a summary of the sensor equipment employed in this study for monitoring the electrical and environmental parameters of both the floating and fixed solar systems. The ACS 712 current sensor was used to measure module output current with a full-scale range of 0–5 A, while the CDR-96 digital ammeter and voltmeter panel provided accurate current and voltage readings up to 100 V and 10 A. For thermal monitoring, the DS18B20 digital temperature sensor was utilized to measure internal module temperatures between −55 °C and +125 °C, while a K-type thermocouple was used to monitor surface and ambient temperatures, operating within −40 °C to +105 °C. Wind speed was assessed using an ABS-cased anemometer rated from wind scale 0 to 16, allowing estimation of environmental wind load impact on the floating structure. In addition to these sensors, solar irradiance was continuously measured using a pyranometer (Model JDA-W). The device features a measurement range of 0–2000 W/m^2, with a resolution of 1 W/m^2 and an accuracy of ±0.05% F.S. ± 2 digits. This pyranometer was used to monitor the real-time irradiance incident on the solar modules, providing essential reference data for evaluating the performance of both the floating and fixed PV systems. A Graphtec GL220 data logger was employed to capture and record all sensor signals, capable of measuring analog voltage (20 mV to 50 V), thermocouple-based temperatures (−200 °C to +100 °C), and relative humidity (0–100% RH) via external modules. The integrated system enabled high-resolution, multi-channel data acquisition at 20 s intervals, providing a robust dataset for performance analysis under varying climatic conditions. The above results are compiled into the power generation curve graphs shown in Figures 11 and 12.

Table 3. Specifications of sensors and measurement equipment.

Item	Sensor/Device	Model	Accuracy/Resolution	Measurement Range
1.	Current sensor	ACS712	27 mV/A	0–5 A
2.	Ammeter	CDR-96	±0.5% F.S., ±2 digits/ Voltage: 0.01 V Current: 0.01 A Power: 0.1 W Capacity: 0.01 Ah Energy: 0.01 Wh	100 V/10 A
3.	Temperature element	DS18B20	±0.5 °C/0.0625 °C	−55 °C to +125 °C
4.	Thermocouple	K-type	±2.2 °C or ±0.75% FS	−40 °C to +105 °C
5.	Anemometer	ABS type	±3%/±0.1 m/s	Wind Scale 0–16
6	Pyranometer	JDA-W	±0.05% F.S., ±2 digits/ 1 W/m^2	0–2000 W/m^2
7.	Data logger	GL220	V: ±0.1% FS, T: ±0.5 °C H: ±5%RH/0.1%RH	V: 20 mV–50 V T: −200 °C–100 °C H: 0–100%

In Figure 11a, the solar irradiance profile under clear-sky conditions is illustrated. The irradiance increased steadily after sunrise, reaching a peak of approximately 870–900 W/m^2 around midday, and then gradually declined toward sunset. This stable irradiance curve reflects typical sunny-day behavior and provides the reference baseline for evaluating system performance. Observing the curves in Figure 11b, it is clear that the temperature

of the fixed solar module (Fixed_T (°C)) is generally higher than that of the floating system (FPV_T (°C)), with a peak temperature reaching 57.4 °C at 12:26. In contrast, the temperature of the floating system's module (FPV_T (°C)) remains consistently below 45 °C. Additionally, the voltage (FPV_V (V)) and current (FPV_A (A)) curves of the floating system, shown in Figure 11c, exhibit higher amplitudes compared to those of the fixed system (Fixed_V (V) and Fixed_A (A)). During the period from 13:44 to 15:09, there was noticeable shading, resulting in a significant drop in both voltage and current. In terms of wind speed, the data shows significant variation due to the mild breeze on the day of testing, as indicated by the wind curve in Figure 11c, which did not reach the wind speed protection activation threshold of 8.0 m/s (0.3 V). Figure 11d illustrates the power output curves of the floating solar-tracking system (FPV) and the fixed-tilt system under mixed weather conditions, including a clear and sunny afternoon. The FPV system achieved a peak output of 11.53 W, significantly surpassing the fixed system's peak of 8.72 W, yielding a 32.22% increase in power generation. This improvement is attributed to the system's dual-axis solar tracking and the active spray-cooling mechanism, which maintained the solar module temperature below 45 °C, mitigating thermal losses. During the peak sunlight period, field measurements indicated that the incident solar irradiance exceeded 1000 W/m^2, providing ideal conditions for evaluating system performance. The FPV system's ability to track the sun's position in real time enabled it to fully utilize the high irradiance levels, resulting in near-maximum output relative to the module's rated capacity. These results confirm that under optimal environmental conditions, the proposed FPV system demonstrates superior energy harvesting capabilities compared to fixed installations, particularly in high-radiation coastal regions like Penghu. On the day of testing, the total power accumulation for the ground-fixed system was 8.90 Wh, while the floating system accumulated 11.14 Wh. The power generation difference between the two systems was 25.17%. It is indicated by the data that the developed system generates more electricity and is more suitable for independent power supply in cage aquaculture systems.



(**a**)

Figure 11. *Cont.*

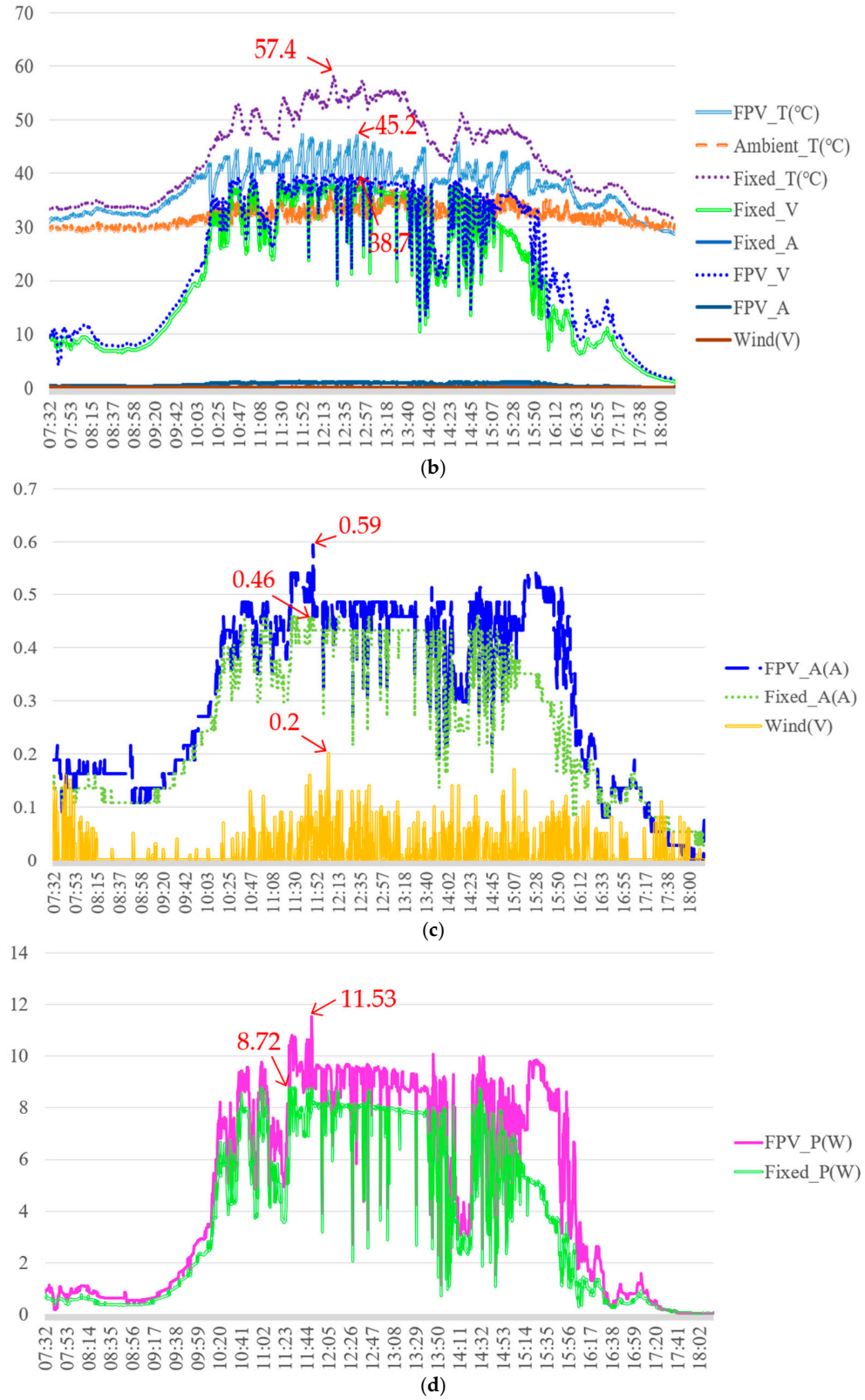
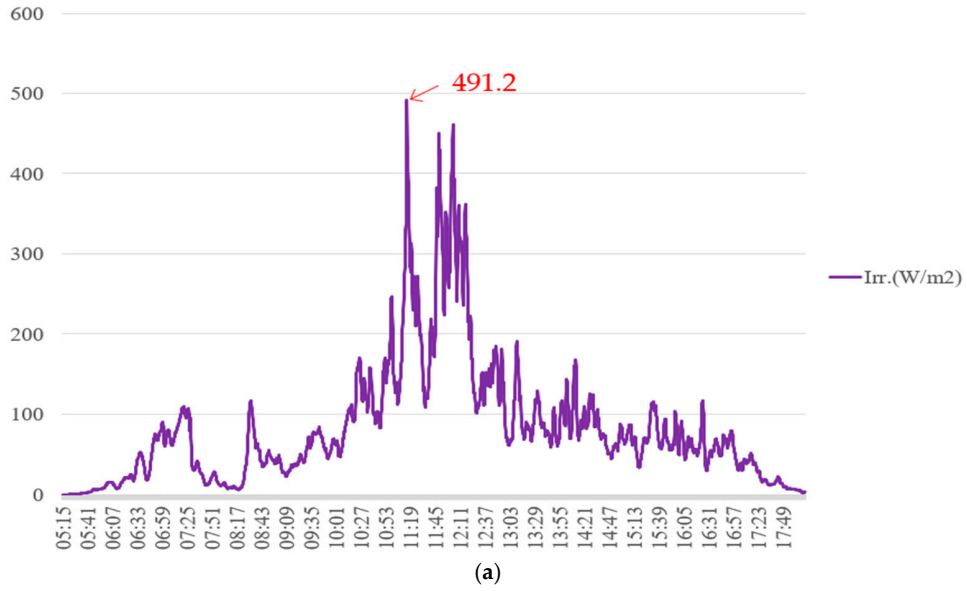


Figure 11. Sunny-day performance of the FPV solar-tracking system: (**a**) Solar irradiance; (**b**) System-parameter traces; (**c**) Expanded view; (**d**) Power-generation curves.

To further evaluate the system's wind-resistance capability, a daytime period with overcast skies and strong winds was selected for testing. The measured curves are shown in Figure 12. On that day, there was light rain in the morning, after which it remained cloudy all day. In Figure 12a, the solar irradiance profile under cloudy conditions is

presented. Unlike the clear-sky case shown in Figure 11a, where irradiance smoothly increased after sunrise to a stable midday peak of about 780–880 W/m^2, the cloudy-day profile exhibits significant fluctuations. The irradiance rose gradually in the morning, but around 10:30–12:00 it showed multiple sharp peaks and deep dips, with a maximum of about 491.2 W/m^2. During the afternoon, the irradiance remained highly variable and mostly below 200 W/m^2, before declining toward sunset. This unstable pattern reflects the intermittent shading effects of passing clouds, highlighting the contrast with the stable sunny-day behavior. In Figure 12b, the plotted curves for both the Fixed and FPV systems—showing voltage and temperature—are all much lower than those in Figure 11b. The Fixed_V and FPV_V curves nearly overlap because the floating system could not track the sun's position, and the high wind speed forced the system to reduce the solar panel's tilt angle to its minimum (nearly horizontal), producing this result. Figure 12c separates and displays the current and wind-speed curves from both systems in Figure 12b. It is evident from these curves that strong winds prevailed on the test day, with an average wind speed of approximately 6.75 m/s (0.25 V). The system is configured such that when wind speed reaches 8.0 m/s (0.3 V)—indicated by the pink dashed line—the solar panel's tilt angle is lowered to its minimum. Figure 12d presents the power output curves of the fixed system and the floating solar-tracking system (FPV) under overcast and high-wind conditions. Due to limited solar irradiance and activation of the wind-protection mechanism, the FPV system was forced to operate at a minimal tilt angle, thereby restricting its tracking capability. Despite this, the FPV system still achieved a higher peak power of 6.14 W, compared to 4.84 W from the fixed panel. This demonstrates that even in suboptimal conditions, the FPV system maintained a performance advantage of approximately 26.86% over the fixed setup. The result highlights the effectiveness of the system's structural design and control strategy in maintaining superior output while protecting against excessive wind loading. In terms of energy yield, the FPV system generated a total of 3.83 Wh, while the fixed system produced 2.73 Wh over the same test period. This represents an increase of approximately 40.29% in total energy output, demonstrating that the floating system maintained a significant advantage even under suboptimal conditions. These results validate the effectiveness of the system's control logic and mechanical design in balancing energy performance and structural safety during adverse weather.



(**a**)

Figure 12. *Cont.*

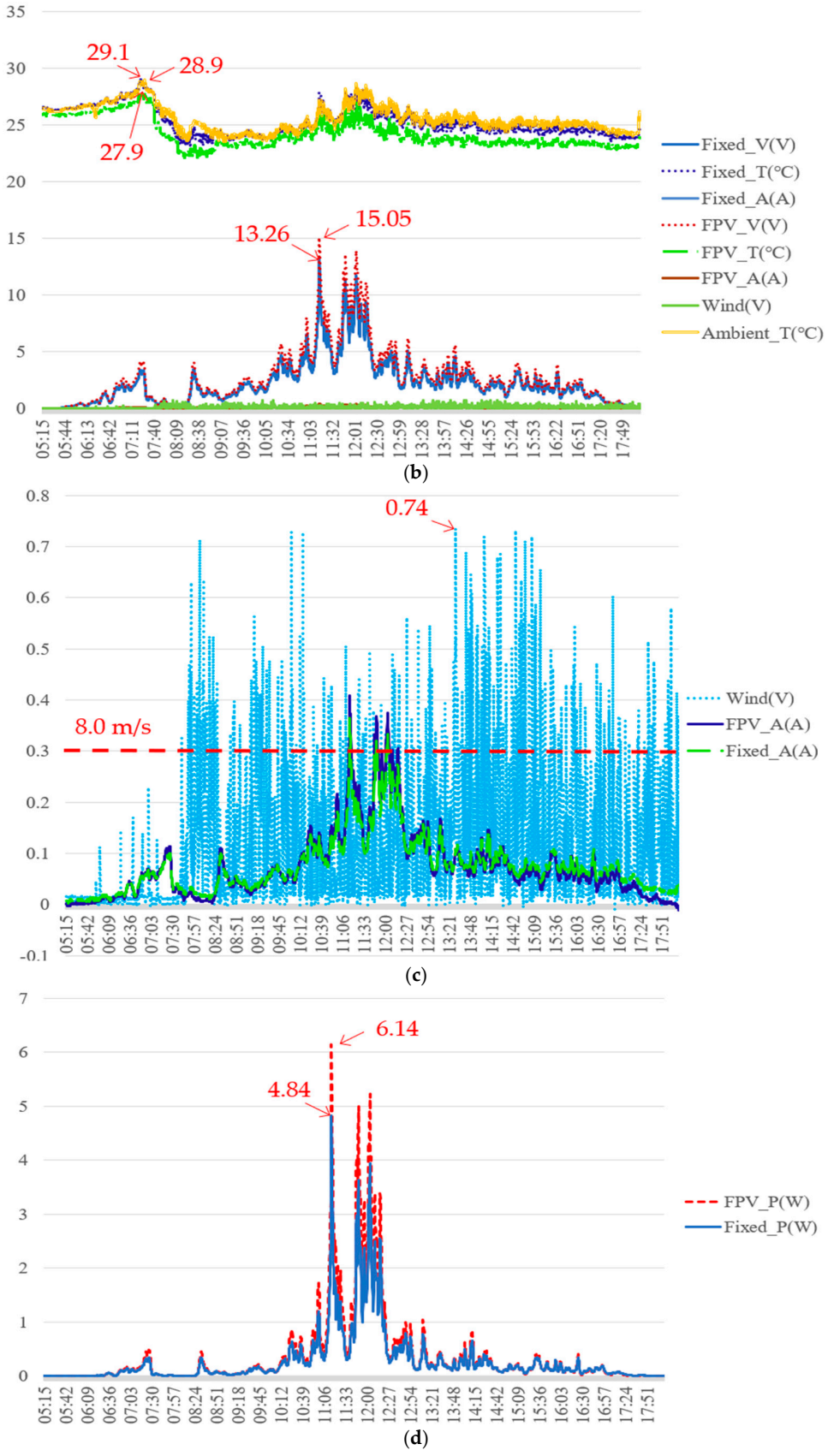


Figure 12. Overcast-day performance of the floating solar-tracking system: (**a**) Solar irradiance; (**b**) System-parameter traces; (**c**) Expanded view of current and wind-speed signals; (**d**) Power-generation curves.

Table 4 presents the normalized energy yield of the 10 Wp PV module under two different weather conditions. On a sunny day, the module produced 11.14 Wh, equivalent to 1.114 kWh/kWp or 0.118 kWh/m^2/day. Under cloudy–windy conditions, the yield decreased to 3.83 Wh, corresponding to 0.383 kWh/kWp or 0.041 kWh/m^2/day. Although these values are lower than theoretical expectations (~0.5 kWh/m^2/day for ~10% efficiency under 5 kWh/m^2 solar irradiation), the discrepancy can be attributed to the absence of MPPT, additional resistive and thermal losses, suboptimal tilt alignment, and the relatively small module area. These limitations are typical in laboratory-scale tests and reasonably explain the lower observed yield.

Table 4. Normalized daily energy yield of the 10 Wp PV module (area: 0.0945 m^2) under different weather conditions.

Weather Condition	Energy Output (Wh)	Normalized Yield (kWh/kWp)	Normalized Yield (kWh/m^2/Day)
Sunny day	11.14	1.114	0.118
Cloudy and windy	3.83	0.383	0.041

Table 5 summarizes the estimated energy loss distribution of the FPV test system under baseline conditions (without spray cooling). Thermal losses were estimated at 15–20%, based on the module temperature rise of 25–35 °C above STC and the manufacturer's temperature coefficients (−0.33%/°C for voltage and +0.08%/°C for current, corresponding to an overall power coefficient of approximately −0.25% to −0.45%/°C). Since the PV module was directly connected to a 40 Ω resistive load, no inverter-related losses were present, while wiring and connection losses were estimated at 2–3% and mechanical factors such as minor shading and mounting tolerance accounted for 1–2%. The net DC output to the load was therefore about 75–80%. After activating the spray cooling system, the thermal losses were significantly reduced, which explains part of the observed +40.29% performance improvement. The overall enhancement, however, exceeded the thermal loss estimate, as additional gains were realized through surface cleaning effects of the spray and improved irradiance capture under solar tracking conditions.

Table 5. Estimated energy loss breakdown of the FPV test system (without spray cooling).

Loss Category	Estimated Share	Notes
Thermal loss	15–20%	Module surface $\Delta T \approx 25$–35 °C, coeff. −0.45%/°C
Wiring and connectors	2–3%	Cable/connection resistance
Mechanical factors	1–2%	Minor shading, mounting tolerance
Inverter	Not applicable	Direct resistive load (40 Ω)
Net output to load	~75–80%	Measured DC output

Table 6 summarizes the experimental performance of the proposed floating PV platform under different operating conditions. The system integrates dual-axis solar tracking, spray-cooling triggered at 45 °C, and a wind-protection mechanism activated at 8.0 m/s (≈0.30 V). Field tests showed that, compared with a fixed-tilt reference, the FPV module achieved 11.53 W peak power and 11.14 Wh daily energy on a sunny day, yielding a +25.17% gain. Under overcast and high-wind conditions, the system delivered 3.83 Wh, corresponding to a +40.29% performance increase, while maintaining module temperature below 45 °C. The modular controller, equipped with multi-sensor inputs (temperature,

wind speed, voltage/current) and supported by a 12 V/10 Ah storage unit, enabled stable autonomous operation and buffered intermittency during wind-protection events. These results confirm that the combined tracking–cooling–windproof architecture effectively enhances both energy yield and mechanical reliability in marine aquaculture environments.

Table 6. Performance improvements of the proposed FPV system compared with a fixed-tilt reference module.

System Feature	Condition/Threshold	Performance Gain/Effect
Floating PV (FPV) module	Compared to fixed-tilt reference	+25.17% energy gain
Spray-cooling subsystem	Module temperature > 45 °C (on)/<35 °C (off)	+40.29% performance increase
Wind-protection mechanism	Triggered at 8.0 m/s (≈0.30 V)	Enhanced system stability under strong wind
Solar-tracking control	Continuous operation (20 s interval)	Improved alignment, higher power output

Table 7 summarizes the key performance specifications of the batteries used in the proposed hybrid energy storage system (HESS). The lithium-ion battery model ICR18650-26JM has a nominal voltage and capacity of 10.8 V/5.2 Ah, with a charging range from 8.25 V to 12.6 V and a charging rate of 1C. Its role is to provide a stable 12 V supply, ensuring reliable operation of the driving circuits and protecting sensitive electronic components. In contrast, the lead-acid battery model SCB 6-DZM-20 offers a much larger capacity of 12 V/24 Ah, with a charging range from 10.5 V to 15 V and a charging rate of 0.3C. This battery serves as the primary storage unit, designed to extend system endurance under cloudy or low-irradiance conditions. The complementary use of both batteries highlights the effectiveness of HESS, balancing immediate power delivery with long-term energy storage capability.

Table 7. Performance specifications of the lithium-ion and lead-acid batteries used in the proposed hybrid energy storage system (HESS).

Parameter	Lithium-Ion Battery	Lead-Acid Battery
Model	ICR18650-26JM	SCB 6-DZM-20
Voltage/Capacity	10.8 V/5.2 Ah	12 V/24 Ah
Full/Cut-Off Voltage	12.6 V/8.25 V	15 V/10.5 V
Charging Current	1C	0.3C

Figure 13 illustrates the voltage responses of the lithium-ion and lead-acid batteries under the priority charging strategy. At the beginning of the test, the lithium-ion battery voltage was about 9.28 V and gradually increased during the charging process. During this stage, the lead-acid battery remained idle without receiving charge. Once the lithium-ion battery reached 12 V, the control logic triggered the switching mechanism, terminating its charging and immediately redirecting the solar energy to the lead-acid battery. As a result of this energy transfer, the lead-acid battery voltage exhibited a sudden spike from 12.72 V to 12.88 V, indicating the onset of energy storage. This observation confirms the effectiveness of the priority charging strategy: the system first ensures the lithium-ion battery is fully charged to stabilize the driving circuits, and then directs the excess energy to the lead-acid battery, thereby achieving both reliable operation and long-term energy storage.

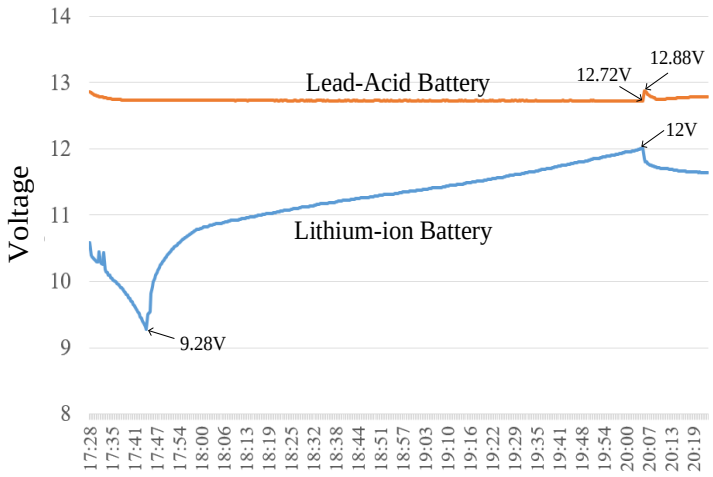
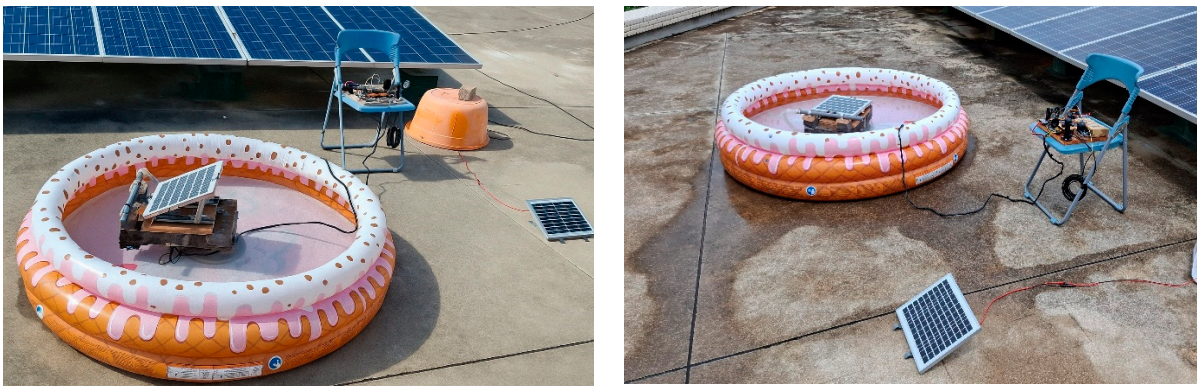


Figure 13. Charging voltage response of lithium-ion and lead-acid batteries with priority control.

Figure 14 illustrates the installation of the developed floating solar-tracking system under different weather conditions. Figure 14a shows the setup used on the testing day described in Figure 11. The configuration includes a 12 V power control module, a wind speed sensor, a 10 W floating solar-tracking panel, and a 10 W fixed solar panel used for performance comparison. Figure 14b presents the setup used on the testing day shown in Figure 12. On that day, due to strong winds, the tilt angle of the solar panel was reduced to its minimum to minimize the risk of overturning.



(**a**) (**b**)

Figure 14. Outdoor test setup of the proposed system (**a**) on a sunny day (**b**) on an overcast day.

5. Conclusions

This study developed and tested an autonomous floating photovoltaic (FPV) system equipped with solar-tracking, spray-cooling, and wind-protection mechanisms to support offshore aquaculture. The experimental validation demonstrated that the proposed system significantly improved energy generation and operational stability when compared with a fixed-tilt reference module.

The main findings are summarized as follows:

- The FPV system achieved an energy gain of +25.17% compared to the fixed-tilt module under the same conditions. This confirms the effectiveness of the dual-axis tracking strategy in maximizing incident irradiance capture and improving overall energy yield.
- With the spray-cooling subsystem, the module operating temperature was effectively reduced, resulting in a performance increase of +40.29% at peak irradiance. This outcome is consistent with the estimated 15–20% thermal loss derived from the manu-

facturer's temperature coefficients (−0.33%/°C for voltage and +0.08%/°C for current), while additional improvement was attributed to surface cleaning and enhanced irradiance capture.

- The wind-protection mechanism successfully triggered at a threshold of 8.0 m/s (≈0.30 V sensor output), enhancing system stability under strong wind conditions. This safety feature reduces the risk of overturning or structural damage and ensures operational reliability during sudden weather fluctuations.
- The solar-tracking control maintained accurate alignment with incident sunlight, improving power output and ensuring the long-term stability of offshore aquaculture operations. This function guarantees stable energy supply for critical aquaculture equipment under variable environmental conditions.
- The hybrid energy storage system (HESS), integrating a lithium-ion battery and a lead-acid battery, demonstrated the effectiveness of a priority charging strategy. During testing, the lithium-ion battery was first charged from 9.28 V to 12 V to stabilize the supply for control circuits. Once this threshold was reached, excess solar energy was immediately redirected to the lead-acid battery, causing its voltage to spike from 12.72 V to 12.88 V. This validated the control logic and confirmed that the system can balance immediate power delivery with long-term storage.

Overall, the integration of solar tracking, spray cooling, wind protection, and a hybrid energy storage strategy provides a practical solution for enhancing FPV performance in coastal marine environments. These findings verify the feasibility of deploying the proposed FPV platform as a sustainable, autonomous, and weather-resilient power source to support offshore aquaculture infrastructure. Future research will therefore explicitly include scalability analysis and long-term durability assessments, with particular attention to the endurance of the energy storage subsystem under cloudy-day or low-irradiance conditions. In addition, long-term monitoring and accelerated life testing will be conducted to evaluate the impacts of biofouling on module transparency, salt-mist corrosion of electrical components, high-humidity exposure and humidity cycling (e.g., condensation and damp-heat effects) on encapsulants, connectors, and mechanical fatigue of the floating platform and actuators. Such efforts will deliver a more comprehensive understanding of system reliability and practical feasibility for extended FPV deployment in marine environments.

Author Contributions: Conceptualization, Y.-D.C.; data curation, J.-H.C. and C.-C.C.; formal analysis, J.-H.C. and C.-C.C.; investigation, J.-H.C. and C.-C.C.; methodology, G.-R.Y.; project administration, Y.-D.C.; resources, Y.-D.C. and G.-R.Y.; software, G.-R.Y.; su-pervision, Y.-D.C.; validation, Y.-D.C.; visualization, J.-H.C. and C.-C.C.; writing—original draft, Y.-D.C.; writing—review and editing, G.-R.Y. All authors have read and agreed to the published version of the manuscript.

Funding: This research received no external funding, and the APC was funded by the authors.

Data Availability Statement: The data presented in this study are not publicly available to facilitate further ongoing research.

Conflicts of Interest: The authors declare no conflict of interest.

References

1. Shih, Y.-C.; Yang, C.-K.; Chiau, W.-Y. Sediment characteristics under and around cobia cage farms at Penghu, Taiwan, as visualized by redox potential and sulfide content profiles using GIS as documentation tool. *J. Aquac. Mar. Biol.* **2016**, *4*, 00101. [CrossRef]
2. Shih, Y.-C. Integrated GIS and AHP for marine aquaculture site selection in Penghu Cove in Taiwan. *J. Coast. Zone Manag.* **2017**, *20*, 1000438. [CrossRef]
3. Shih, Y.-C. Marine environmental management and development strategy for marine aquaculture in Taiwan: Cobia case study. *Adv. Oceanogr. Mar. Biol.* **2018**, *1*, 000503. [CrossRef]

4. Lan, H.-Y.; Afero, F.; Huang, C.-T.; Chen, B.-Y.; Huang, P.-L.; Hou, Y.-L. Investment feasibility analysis of large submersible cage culture in Taiwan: A case study of snubnose pompano (*Trachinotus anak*) and cobia (*Rachycentron canadum*). *Fishes* **2022**, *7*, 151. [CrossRef]
5. Tang, H.-J.; Chiang, W.-S.; Nan, F.-H. Engineering feasibility assessment of cage aquaculture in offshore wind power generation areas in Taiwan. *Sustainability* **2022**, *14*, 11705. [CrossRef]
6. Sievers, M.; Korsøen, Ø.; Warren-Myers, F.; Oppedal, F.; Macaulay, G.; Folkedal, O.; Dempster, T. Submerged cage aquaculture of marine fish: A review of the biological challenges and opportunities. *Rev. Aquac.* **2022**, *14*, 106–119. [CrossRef]
7. Bujas, T.; Koričan, M.; Vukić, M.; Soldo, V.; Vladimir, N.; Fan, A. Review of energy consumption by the fish farming and processing industry in Croatia and the potential for zero-emissions aquaculture. *Energies* **2022**, *15*, 8197. [CrossRef]
8. Vo, T.T.E.; Ko, H.; Huh, J.-H.; Park, N. Overview of solar energy for aquaculture: The potential and future trends. *Energies* **2021**, *14*, 6923. [CrossRef]
9. Vivar, M.; Sharon, H.; Fuentes, M. Photovoltaic system adoption in water related technologies—A review. *Renew. Sustain. Energy Rev.* **2024**, *189*, 114004. [CrossRef]
10. Gorjian, S.; Sharon, H.; Ebadi, H.; Kant, K.; Bontempo Scavo, F.; Tina, G.M. Recent technical advancements, economics and environmental impacts of floating photovoltaic solar energy conversion systems. *J. Clean. Prod.* **2021**, *278*, 124285. [CrossRef]
11. Guo, H.; Wang, X.; Liu, B.; Chan, Z.; Pan, Z.; Chen, L.; Xi, Q.; Zhu, W.; Wu, J.; Cao, G.; et al. Global trends and evolution of aquavoltaics in sustainable aquaculture and energy generation. *Renew. Energy* **2025**, *255*, 123864. [CrossRef]
12. Nisar, H.; Janjua, A.K.; Hafeez, H.; Shakir, S.; Shahzad, N.; Waqas, A. Thermal and electrical performance of solar floating PV system compared to on-ground PV system—An experimental investigation. *Sol. Energy* **2022**, *241*, 231–247. [CrossRef]
13. Manolache, M.; Manolache, A.I.; Andrei, G. Floating Solar Energy Systems: A Review of Economic Feasibility and Cross-Sector Integration with Marine Renewable Energy, Aquaculture and Hydrogen. *J. Mar. Sci. Eng.* **2025**, *13*, 1404. [CrossRef]
14. Segbefia, O.K. Temperature profiles of field-aged photovoltaic modules affected by optical degradation. *Heliyon* **2023**, *9*, e19566. [CrossRef] [PubMed]
15. Sutanto, B.; Indartono, Y.S.; Wijayanta, A.T.; Iacovides, H. Enhancing the performance of floating photovoltaic system by using thermosiphon cooling method: Numerical and experimental analyses. *Int. J. Therm. Sci.* **2022**, *180*, 107727. [CrossRef]
16. Siecker, J.; Kusakana, K.; Numbi, B.P. A review of solar photovoltaic systems cooling technologies. *Renew. Sustain. Energy Rev.* **2017**, *79*, 192–203. [CrossRef]
17. Cazzaniga, R.; Cicu, M.; Rosa-Clot, M.; Rosa-Clot, P.; Tina, G.; Ventura, C. Floating photovoltaic plants: Performance analysis and design solutions. *Renew. Sustain. Energy Rev.* **2018**, *81*, 1730–1741. [CrossRef]
18. Canbaz, A.; Karakoyun, Y.; Uzmuş, H. An experimental performance analysis of canal-mounted photovoltaic systems regarding energy production and water conservation. *Sol. Energy* **2025**, *299*, 113749. [CrossRef]
19. Ramanan, C.J.; Lim, K.H.; Kurnia, J.C. Thermal behavior of floating photovoltaics: A comparison of performance at varying heights and benchmarking against land-based photovoltaics. *Appl. Energy* **2025**, *388*, 125642. [CrossRef]
20. Tashtoush, B.; Al-Oqool, A. Factorial analysis and experimental study of water-based cooling system effect on the performance of photovoltaic module. *Int. J. Environ. Sci. Technol.* **2019**, *16*, 3645–3656. [CrossRef]
21. Hairuddin, H.S.S.; Yahaya, J.A.F. Integrated IoT monitoring, tracking, and cleaning system for PV floating structures. *Evol. Electr. Electron. Eng.* **2023**, *4*, 115–125.
22. Anwar, M.; Singh, M.; Singh, H.A.; Rajbhar, S.; Pillai, A.G. Solar tracking system with automatic panel cleaning mechanism for efficient power generation. *Int. J. Creat. Res. Thoughts* **2023**, *11*, b754–b756.
23. Kodamanchili, R.; Devadass, P. Sun tracking automatic panel cleaning mechanism & solar panel with GSM based energy billing system. *Int. Res. J. Eng. Technol.* **2020**, *7*, 1304–1307.
24. Fatah, A.; Menzri, F.; Lekmine, A.; Benlaloui, I.; Boutabba, T.; Fezzani, A. Control of water pumping system based on floating photovoltaic system with a solar tracking control. In Proceedings of the 2023 International Conference on Electrical Engineering and Advanced Technology (ICEEAT), Batna, Algeria, 5–7 November 2023.
25. Huang, Y.-C.A.; Huang, S.-C.; Meng, P.-J.; Hsieh, H.J.; Chen, C.-A. Influence of strong monsoon winds on the water quality around a marine cage-culture zone in a shallow and semi-enclosed bay in Taiwan. *Mar. Pollut. Bull.* **2012**, *64*, 851–860. [CrossRef]
26. Bettahar, F.; Sabrina, A.; Achour, B. Enhancing PV systems with intelligent MPPT and improved control strategy of Z-source inverter. *Power Electron. Drives* **2024**, *9*, 1–20. [CrossRef]
27. Jed, M.E.H.; Ihaddadene, R.; Ihaddadene, N.; Elhadji Sidi, C.E.B.; El Bah, M. Performance analysis of 954,809 kWp PV array of Sheikh Zayed solar power plant (Nouakchott, Mauritania). *Renew. Energy Focus* **2020**, *32*, 45–54. [CrossRef]
28. Natarajan, S.K.; Kumar, A.; Mohamed, R.; Rathna, R.; Mondal, S.; Suraparaju, S.K. Design and development of dual axis sun tracking system for floating PV plant. *IOP Conf. Ser. Earth Environ. Sci.* **2019**, *312*, 012001. [CrossRef]

29. Jamil, N.A.A.; Jumaat, S.A.; Salimin, S.; Abdullah, M.N.; Nor, A.F.M. Performance enhancement of solar powered floating photovoltaic system using Arduino approach. *Int. J. Power Electron. Drive Syst.* **2020**, *11*, 651–657. [CrossRef]
30. Ilas, M.A.M.; Islam, S.Z. Performance comparison of monocrystalline PV module using floating and non-floating method. *Evol. Electr. Electron. Eng.* **2021**, *2*, 106–112.

Disclaimer/Publisher's Note: The statements, opinions and data contained in all publications are solely those of the individual author(s) and contributor(s) and not of MDPI and/or the editor(s). MDPI and/or the editor(s) disclaim responsibility for any injury to people or property resulting from any ideas, methods, instructions or products referred to in the content.